

CrossMark
click for updatesCite this: *RSC Adv.*, 2016, 6, 20001

A controlled, template-free, and hydrothermal synthesis route to sphere-like α -Fe₂O₃ nanostructures for textile dye removal

Mostafa Y. Nassar,* Ibrahim S. Ahmed, Talaat Y. Mohamed and Mai Khatab

Iron carbonate nanospheres were synthesized *via* hydrothermal treatment of aqueous solutions of iron sulfate, ascorbic acid and ammonium carbonate with a molar ratio of 1 : 1 : 3, respectively, at 140 °C for 1.5 h. Pure α -Fe₂O₃ nanoparticles with an average crystallite size of 10.5–32 nm were produced by thermal decomposition of FeCO₃ at 400–600 °C for 2 h. The compositions of the products were identified by means of XRD, FE-SEM, HR-TEM, FT-IR, BET, zeta potential and thermal analysis. The adsorption properties of α -Fe₂O₃ were evaluated using reactive red 195 (RR195) dye. Various parameters influencing the adsorption process were investigated, using a batch technique. The results show that α -Fe₂O₃ nanoparticles show good adsorption capacity and the dye removal percentage reaches about 98.77% in 10 min. Plus, increasing the surface area of the α -Fe₂O₃ nanoparticles from 107.7 to 165.6 m² g⁻¹ increases the adsorption capacity from 4.7 to 20.5 mg g⁻¹. Moreover, the adsorption data fit the Langmuir isotherm model well and the thermodynamic parameters exhibited an endothermic and spontaneous nature for the adsorption of RR195 dye on the hematite adsorbent.

Received 7th December 2015

Accepted 10th February 2016

DOI: 10.1039/c5ra26112k

www.rsc.org/advances

1. Introduction

Over the past few years, water pollution has been considered as one of the major threats to our world because it results in an imbalance and significant alterations in the hydrological cycle which in turn cause many health problems and may even lead to death.¹ Synthetic organic dyes mainly produced from different industries (such as leather, paper, textile, plastic, refineries, and chemical) are mostly toxic, carcinogenic, and stable against photodegradation and these dyes along with heavy metals induce water pollution.^{2,3} Hence, the wastewater generated from various industries has to be treated using an appropriate method before discharge, in order to get rid of these problems. There are several physical and chemical methods have been proposed for organic dye removal from wastewaters such as photodegradation, precipitation, filtration, coagulation, ion exchange, reverse osmosis, adsorption, *etc.*^{4–8} Among all the proposed attempts for dye removal, adsorption is still considered the most appropriate method in this concern due to its simplicity, economic applicability, high efficiency, and nonexistence of harmful species. Due to the high surface area of the nanomaterials, several research groups have focused their efforts on synthesizing of nanosized oxides using different routes and proposing them as good adsorbents.^{2–14}

On the other hand, nanosized iron oxides have recently received a considerable interest of several research groups as efficient adsorbents for the decontamination purpose of wastewater.^{8,15,16} Among nano-sized iron(III) oxides, hematite, α -Fe₂O₃, is the most important and thermodynamically stable form under ambient conditions.¹⁷ Due to its stability, non-toxicity, high efficiency, and inexpensive nature, hematite has been used in different applications such as gas sensors, pigments, electrode materials, catalysts, magnetic resonance imaging, clinical therapy, magnetic materials, printing inks, ferrofluids, and water treatment.^{18–23} These interesting properties and applications stimulated many material and inorganic researchers to direct their efforts to synthesize α -Fe₂O₃ with different morphologies and particle sizes.^{24–27} As a consequence, several methods such as micro-emulsion, sol-gel, hydro/solvothermal, microwave-assisted solvothermal, ultrasonic precipitation, mechanochemical, thermal decomposition, and sono-electrochemical anodization have been developed for the synthesis of nanosized α -Fe₂O₃ structures.^{27–34} Although the methods that have been reported for synthesis of hematite are a lot, it is still a big challenge to have a facile and inexpensive methodology to control the morphology and particle size of the hematite nanostructures. So far, the hydrothermal technique still has the priority over the most synthetic methods due to its low-cost, simplicity, and varying morphologies of products.¹¹ Plus, there are different parameters; such as temperature, time, solvents, and precursors, for the hydrothermal process the researcher can tune them to control the purity, particle size, and morphology of the products. However, we have reported on the

Chemistry Department, Faculty of Science, Benha University, Benha 13518, Egypt.
E-mail: m_y_nassar@yahoo.com; m_y_nassar@fsc.bu.edu.eg; Fax: +20 133222578;
Tel: +20 1068727555

hydrothermal synthesis of CoCO_3 microspheres and their thermal conversion into cobalt oxide nanoparticles.^{5,11,12} One of the most important aspects of producing metal oxide nanoparticles through thermal conversion of metal carbonates is the formation of nano-pores due to the release of carbon dioxide from metal carbonate during the thermal decomposition step which results in novel nanostructures with relatively large specific surface area. Reports on similar synthetic routes for producing $\alpha\text{-Fe}_2\text{O}_3$ via thermal decomposition of hydrothermally prepared ferrous carbonate are still limited.^{34–37} In such, Liu *et al.* reported on synthesis of FeCO_3 microspheres using a surfactant-assisted hydrothermal reaction of iron chloride and urea.³⁴ Plus, Xuan *et al.* prepared FeCO_3 with still large particle size through the hydrothermal reaction of the same iron salt with different carbonate source (NaCO_3).³⁵ Also, Yang *et al.* reported on preparation of FeCO_3 microspheres using the relatively inexpensive iron sulfate salt via its hydrothermal treatment with urea but they used relatively large quantity of ascorbic acid in their procedure and their FeCO_3 have large particle size.³⁶ However, an extensive study on the hydrothermal treatment of FeSO_4 and $(\text{NH}_4)_2\text{CO}_3$ to produce FeCO_3 with smaller particle size using smaller quantity of ascorbic acid at relatively low temperature has not been reported so far.

In the current work, as a continuation to our previous study,^{5,11,12} a facile hydrothermal synthesis was adopted, for the first time, to synthesize spherical FeCO_3 nanoparticles in high yield by the reaction of iron sulfate and ammonium carbonate, as an inexpensive carbonate source, in presence of ascorbic acid. Different conditions affecting the synthesis process such as reaction temperature, molar ratio of the reactants, and reaction time have been investigated. Pure $\alpha\text{-Fe}_2\text{O}_3$ nanoparticles are easily produced by thermal conversion of the as-prepared FeCO_3 in air. The as-prepared materials have been characterized by means of thermal analysis and different spectroscopic tools. The applicability of the as-prepared hematite nanoparticles was investigated for the removal of Reactive Red 195 dye (RR195) as a pollutant model from aqueous phase.

2. Experimental

2.1. Chemicals and reagents

Unless otherwise stated, all chemicals and reagents in this work were of analytical grade and they were purchased and utilized as received without further purification: iron sulfate ($\text{FeSO}_4 \cdot 7\text{H}_2\text{O}$; Sigma-Aldrich), ascorbic acid ($\text{C}_6\text{H}_8\text{O}_6$; Sigma-Aldrich), and ammonium carbonate ($(\text{NH}_4)_2\text{CO}_3$; Fluka), Reactive Red 195 dye (RR195) ($\text{C}_{31}\text{H}_{19}\text{ClN}_7\text{O}_{19}\text{S}_6\text{Na}_5$; Rushabh chemicals industries, India).

2.2. Preparation of FeCO_3 and $\alpha\text{-Fe}_2\text{O}_3$ nanoparticles

In a typical preparation procedure: iron sulfate (1.95 g, 7 mmol, 1 eq.) and ascorbic acid (1.23 g, 7 mmol, 1 eq.) were dissolved in 45 mL distilled water under stirring. To the stirring solution, an aqueous ammonium carbonate solution (2.016 g, 21 mmol, 3 eq.) (25 mL) was added and the stirring was continued for 10

min. Afterwards, the produced reaction mixture was then transferred into a 100 mL Teflon-lined autoclave which in turn was placed in an electric oven maintained at 140 °C for 1.5 h. The autoclave was naturally cooled and the precipitate (FeCO_3) was centrifuged and washed several times with distilled water and ethanol and dried in an oven at *ca.* 60 °C overnight. However, in order to obtain the previously mentioned optimum conditions, different experimental parameters affecting this hydrothermal reaction such as temperature (120–160 °C), time (0.5–3 h), and molar ratio (iron sulfate : ascorbic acid : ammonium carbonate; 1 : - : 6, 1 : 0.5 : 6, 1 : 1 : 6, 1 : 2 : 6, 1 : 3 : 6, 1 : 1 : 1, 1 : 1 : 2, 1 : 1 : 3, and 1 : 1 : 6) have been investigated.

The nanosized iron(II) carbonate product prepared at the optimized conditions of the hydrothermal process was calcined at 400, 500, or 600 °C for 2 h in air to produce $\alpha\text{-Fe}_2\text{O}_3$ nanoparticles – with different crystallite sizes – denoted as $\text{Fe}_2\text{O}_3\text{-400}$, $\text{Fe}_2\text{O}_3\text{-500}$, and $\text{Fe}_2\text{O}_3\text{-600}$, respectively.

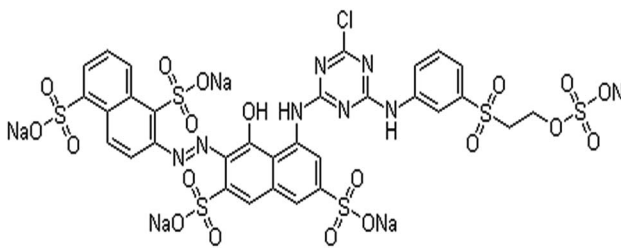
2.3. Characterization

The crystallinity and phase purity of the as-prepared products were identified via powder X-ray diffraction (XRD) by using 18 kW diffractometer (Bruker; model D8 Advance) with monochromated Cu-K α radiation (λ 1.54178 Å). Using a field emission scanning electron microscope (FE-SEM) connected with a microscope (JEOL JSM-6500F), FE-SEM images were taken. The high resolution transmission electron microscope (HR-TEM) images were obtained on a transmission electron microscope (JEM-2100) at an accelerating voltage of 200 kV by dispersing the samples in ethanol ultrasonically on a copper grid. FT-IR spectra were recorded on FT-IR spectrometer (Thermo Scientific; model Nicolet iS10) from 4000 to 400 cm^{-1} . The UV-vis spectra of adsorption studies were recorded using a Jasco UV-vis spectrophotometer (Jasco; model v670). The thermal analysis measurements of the as-prepared iron carbonate were carried out on a thermal analyzer instrument (Shimadzu; model TA-60WS) in a nitrogen atmosphere with a heating rate of 15 °C min^{-1} . BET (Brunauer–Emmet–Teller) surface area of the as-synthesized Fe_2O_3 products was performed on Quantachrome (Nova 2000 series, USA) using nitrogen adsorption–desorption measurements. The zeta potential of the nanosized hematite product was measured using a Zetasizer nano series meter (Nano ZS, Malvern, UK).

2.4. Adsorption experiments

The adsorption experiments were carried out in a batch method performed under a continuous magnetic stirring using Reactive Red 195 dye (RR195) as an adsorbate model, Table 1. The RR195 dye is a commercial product and it is used as received from Rushabh chemicals industries company, India, without further purification. Different experimental factors affecting the adsorption process such as dye solution pH (0.5–9), contact time (5–70 min), temperature (25–45 °C), initial concentration (10–50 ppm) and salt effect, have been investigated. In a typical batch experiment, 50 mL of an aqueous RR195 dye solution of a desired concentration was prepared by suitable dilution of

Table 1 Characteristics and chemical structure of reactive red 195 dye

Dye name	Reactive red 195, RR195
Chemical structure	
Molecular formula	C ₃₁ H ₁₉ ClN ₇ O ₁₉ S ₆ Na ₅
Chemical class	Azo derivative compound
λ_{max}	542 nm
Type	Anionic dye
Solubility	Water soluble
C.I. number	Reactive red 195

a stock solution and by using 0.1 mol L⁻¹ HCl or NaOH aqueous solutions the pH of the solution was adjusted. Afterwards, a known quantity (0.1 g) of dry α -Fe₂O₃ nanoparticles was added and the produced suspension in the conical flask was then allowed to magnetically stir (400 rpm) for a definite time at room temperature. According to the experimental conditions under investigation, the temperatures and concentrations of the adsorbate were varied. After a predetermined time of stirring, an aliquot was taken out of the flask and the adsorbent was separated by centrifugation at 4000 rpm for about 4 min and then the concentration of the remaining dye in the supernatant solution was determined using UV-vis spectrophotometer. It is noteworthy that analysis of the remaining dye concentration in the supernatant was carried out using a previously constructed calibration graph. The obtained data were used to calculate the adsorption capacities (q_t , mg g⁻¹) and the dye removal efficiencies (% removal) using eqn (1) and (2).

$$q_t = \frac{V(C_0 - C_t)}{m} \quad (1)$$

$$\% \text{ removal} = \frac{(C_0 - C_t)}{C_0} \times 100 \quad (2)$$

where C_0 and C_t are the RR195 dye concentrations in mg L⁻¹ at time = 0 and t respectively in solution, V is the volume of dye solution (L), and m is the mass of dry α -Fe₂O₃ adsorbent (g).

3. Results and discussion

3.1. Hydrothermal synthesis and characterization of FeCO₃ nanospheres

Hydrothermal reactions of iron sulfate and ammonium carbonate in presence of ascorbic acid have been investigated in order to prepare pure iron carbonate. Fig. 1(a) exhibits the XRD pattern of FeCO₃ nanospheres synthesized by the hydrothermal treatment of aqueous solutions of iron sulfate, ammonium carbonate and ascorbic acid at the optimal conditions: Fe²⁺ : ascorbic acid : CO₃²⁻ molar ratio of 1 : 1 : 3, 1.5 h reaction time, and 140 °C reaction temperature. All the diffraction

peaks can be indexed well to a pure rhombohedral phase of FeCO₃ which is in consistent with the standard patterns of iron carbonate (space group $R\bar{3}c$, JCPDS card 83-1764).³⁷ No other characteristic peaks corresponding to iron oxides or even other impurities have been observed. The average crystallite size (D) of the as-prepared FeCO₃ was found to be 22 nm which was calculated using the Debye–Scherrer formula:³⁸

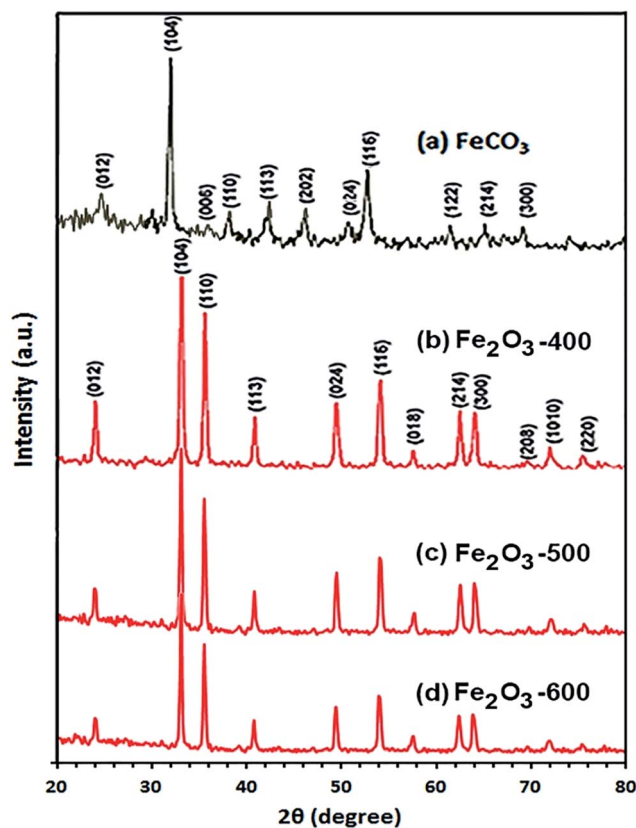


Fig. 1 XRD patterns of the as-synthesized FeCO₃ (a), and α -Fe₂O₃ nanoparticles produced at: 400 °C (b), 500 °C (c), and 600 °C (d).

$$D = 0.9\lambda/\beta \cos \theta_B$$

where λ is the X-ray wavelength, β is the full width at half maximum (FWHM) of the diffraction peak and θ_B is the Bragg diffraction angle. Producing of α -Fe₂O₃ nanoparticles, Fig. 1(b), was performed through thermal conversion of the hydrothermally as-synthesized iron carbonate precursor at the optimal condition as will be explained later.

3.1.1. Optimization of the hydrothermal preparation of FeCO₃ nanoparticles. The optimum conditions for preparation of pure iron carbonate have been reached by studying the various reaction conditions influencing the hydrothermal process such as reaction temperature, reaction time and iron sulfate : ascorbic acid : ammonium carbonate molar ratio using the XRD analysis.

3.1.1.1. Effect of temperature. Effect of temperature on the hydrothermal treatment of the reactants has been investigated first and Fig. 2(a)–(c) exhibits the XRD patterns of the hydrothermally produced products using molar ratio of 1 : 3 : 6 for iron sulfate : ascorbic acid : ammonium carbonate, respectively, for 3 h at different temperatures (160, 140, and 120 °C). It can be noticed that the three temperatures produced iron carbonates and the optimum temperature was 140 °C since it gave pure iron carbonate with a moderate crystallite size (80 nm). However, 160 °C temperature gave pure product with very large crystallite size (200 nm), and 120 °C produced the product with very poor crystallinity contaminated with some impurities as indicated from their XRD patterns and appearance of some peaks for some undefined by-products.

3.1.1.2. Effect of reaction time. Fig. 3(a)–(e) reveals the reaction time effect (3, 2, 1.5, 1, and 0.5 h) on the hydrothermal treatment of interest at 140 °C with iron sulfate : ascorbic acid : ammonium carbonate molar ratio of 1 : 3 : 6. The results indicated that the optimum reaction time was 1.5 h. On the

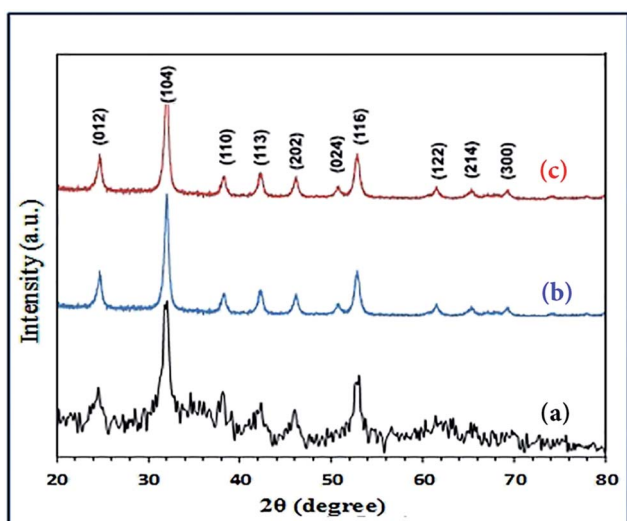


Fig. 2 (a–c) XRD patterns of the FeCO₃ samples prepared under hydrothermal conditions for 3 h with molar ratio of 1 : 3 : 6 for iron sulfate : ascorbic acid : ammonium carbonate, respectively, at different temperatures: 120 (a), 140 (b), and 160 °C (c).

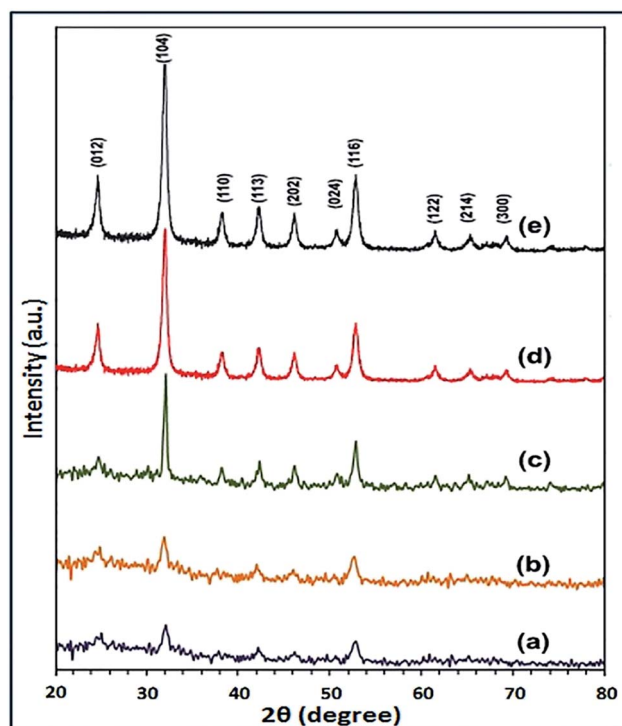


Fig. 3 (a–e) XRD patterns of the samples prepared under hydrothermal conditions with molar ratio of 1 : 3 : 6 for iron sulfate : ascorbic acid : ammonium carbonate, respectively, at 140 °C for 0.5 (a), 1 (b), 1.5 (c), 2 (d), and 3 h (e).

other hand, shorter time (*i.e.* <1.5 h) produced iron carbonate with poor crystallinity and low yield, but longer reaction time gave particles with very large crystallite size. On comparing the optimum temperature and time in the current study with other reported ones for preparing pure iron carbonate, it can easily be seen that we have used lower temperature and shorter time than the reported ones.^{34–36}

3.1.1.3. Effect of ascorbic acid concentration. Ascorbic acid in this study plays a remarkable role since it acts as a reducing agent preventing iron(II) ions from oxidation and its influence on the reaction has been studied. First this hydrothermal treatment has been carried out at 1.5 h reaction time, 140 °C reaction temperature, a fixed Fe²⁺ : CO₃²⁻ molar ratio of 1 : 6 in absence of ascorbic acid, and the XRD pattern of the product is shown in Fig. 4(a). Also, the influence of addition of different quantities of ascorbic acid have been explored by trying different Fe²⁺ : ascorbic acid : CO₃²⁻ molar ratios: 1 : 0.5 : 6, 1 : 1 : 6, 1 : 2 : 6, and 1 : 3 : 6; and the XRD results are depicted in Fig. 4(b)–(e), respectively. Inspection of XRD patterns of the produced products (Fig. 4) reveals that the minimum required equivalents of ascorbic acid are 1 (*i.e.* Fe²⁺ : ascorbic acid : CO₃²⁻ optimum molar ratio is 1 : 1 : 6) and using less equivalents of the ascorbic acid (*i.e.* <1 equivalent) gives iron carbonate with poor crystallinity along with some impurities such as magnetite. It is worthy to mention that in the current hydrothermal treatment smaller quantity of ascorbic acid has been used to produce pure iron carbonate with smaller particle size on comparing to the other reported methods.^{34–36} However,

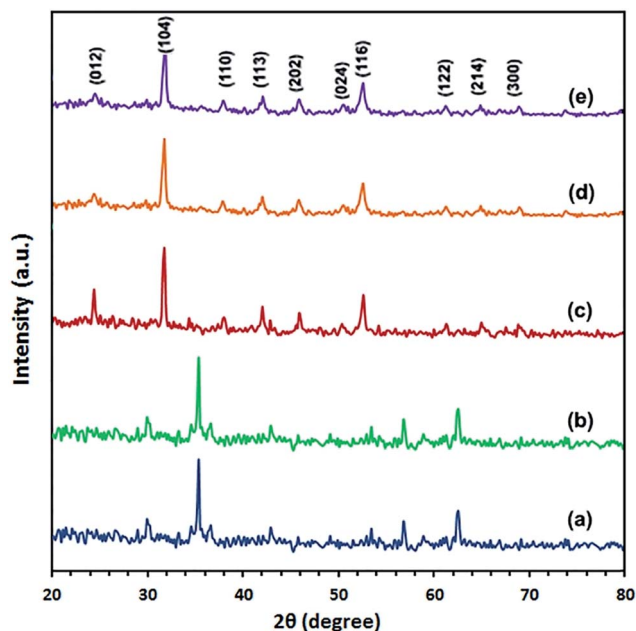
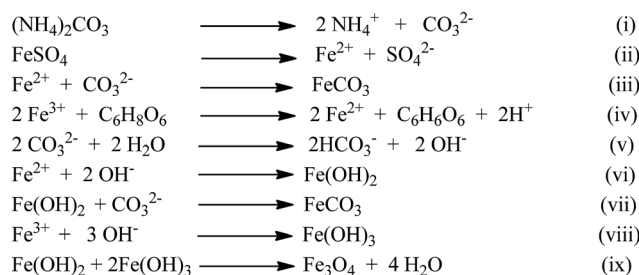


Fig. 4 (a–e) XRD patterns of the samples prepared under hydrothermal conditions with $\text{Fe}^{2+} : \text{CO}_3^{2-}$ molar ratios of 1 : 6 (a), and with $\text{Fe}^{2+} : \text{ascorbic acid} : \text{CO}_3^{2-}$ molar ratios of 1 : 0.5 : 6 (b), 1 : 1 : 6 (c), 1 : 2 : 6 (d), and 1 : 3 : 6 (e), at 140 °C for 1.5 h.

the mechanism of the current hydrothermal process can be explained according to the proposed Scheme 1 as follows: ammonium carbonate and iron sulfate generate carbonate and iron ions according to reactions (i) and (ii), respectively. At the optimum or higher concentrations of both carbonate ions and ascorbic acid, reactions (iii) and (vii) (Scheme 1) will be the more predominant reactions and accordingly the product will be pure iron carbonate. At lower concentration of ascorbic acid, Fe^{3+} ions (produced from oxidation of Fe^{2+} during mixing or heating) will not be completely reduced to Fe^{2+} ions (reaction (iv)) and in turn Fe^{3+} ions will react with OH^- (which can be generated from reaction (v)) to produce $\text{Fe}(\text{OH})_3$. Thence, there will be a competition between reactions (iii), (vii) and (ix) and the result of that competition will be a mixture of iron carbonate and Fe_3O_4 . Additionally, Fe_3O_4 impurities are by-products generated from the reaction between $\text{Fe}(\text{OH})_3$ (reaction (viii)) and $\text{Fe}(\text{OH})_2$ (reaction (vi)) at the hydrothermal conditions



Scheme 1 Proposed reaction mechanism for formation of FeCO_3 or a mixture of FeCO_3 and Fe_3O_4 .

according to reaction (ix) (Scheme 1) and this is in agreement with the reported data.³⁶

3.1.1.4. Effect of $\text{Fe}^{2+} : \text{CO}_3^{2-}$ molar ratios. Effect of ammonium carbonate concentration has been investigated by keeping Fe^{2+} ion and ascorbic acid concentrations constant and varying the concentration of ammonium carbonate by using the following different molar ratios: 1 : 1 : 1, 1 : 1 : 2, 1 : 1 : 3, and 1 : 1 : 6 for $\text{Fe}^{2+} : \text{ascorbic acid} : \text{CO}_3^{2-}$, respectively, and the XRD patterns of the products are given in Fig. 5(a)–(d), respectively. The obtained results reveal that using lower concentration of CO_3^{2-} anion than 3 equivalents produces by-products along with FeCO_3 with very poor crystallinity. Consequently, it can be concluded that the optimum molar ratio for this template-free hydrothermal reaction is (1 : 1 : 3) for $\text{Fe}^{2+} : \text{ascorbic acid} : \text{CO}_3^{2-}$, respectively.

3.1.2. Morphological study. Fig. 6(Ia and Ib) presents the FE-SEM images of the as-synthesized FeCO_3 nanostructures prepared under the optimized conditions with a low and high magnifications, respectively. It is obvious from the low magnification image, Fig. 6(I), that the iron carbonate product is almost composed of agglomerates of nanospheres and from the high magnification image, Fig. 6(Ib), average size of the nanospheres was estimated to be about 70 nm in the diameter. It is noticeably that pure iron carbonate with smaller particle size (70 nm) has been successfully synthesized hydrothermally on comparing to the previously reported results.^{34–36}

3.1.3. FT-IR study. Fig. 7(a) displays the IR spectrum of the as-synthesized FeCO_3 product and it reveals vibrational absorptions at 1392, 1109, 859, and 735 cm^{-1} attributing to the absorbance of pure iron carbonate product and these stretching vibrations are fingerprint of D_3h symmetry which in turn is an evidence for the presence of carbonate anions in the iron carbonate products.^{5,11,12,39} The weak band appeared at 2457 cm^{-1} may be assigned to the stretching vibration of the carbonate anions.^{5,11,12,40} Plus, the vibrational shoulder observed

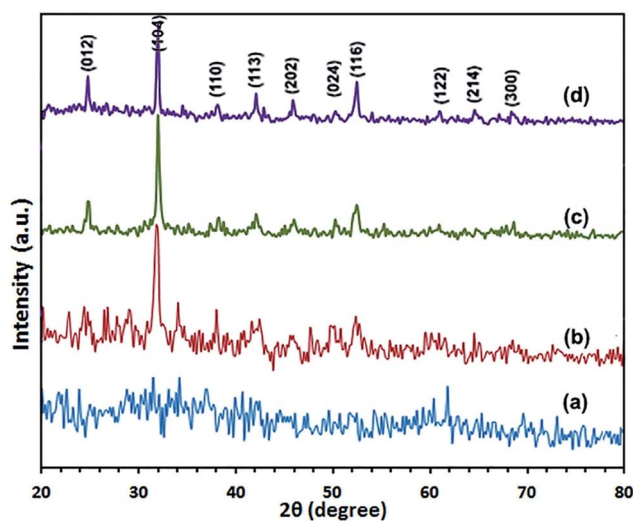


Fig. 5 (a–d) XRD patterns of the samples prepared under hydrothermal conditions with $\text{Fe}^{2+} : \text{ascorbic acid} : \text{CO}_3^{2-}$ molar ratios of 1 : 1 : 1 (a), 1 : 1 : 2 (b), 1 : 1 : 3 (c), and 1 : 1 : 6 (d), at 140 °C for 1.5 h.

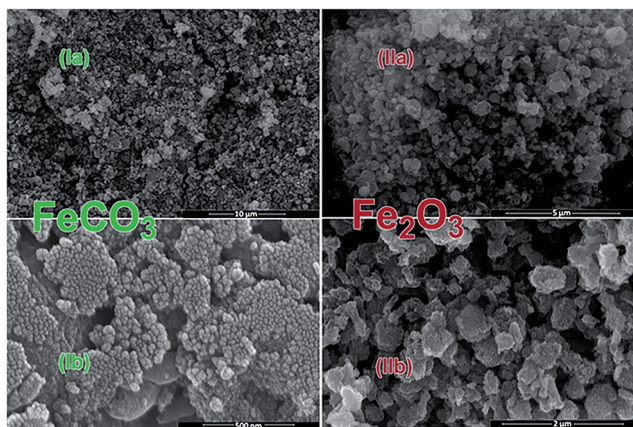


Fig. 6 FE-SEM images for as-synthesized FeCO_3 (Ia, Ib), and $\alpha\text{-Fe}_2\text{O}_3$ produced at 600°C (IIa, IIb); low (Ia, IIa) and high (Ib, IIb) magnification images.

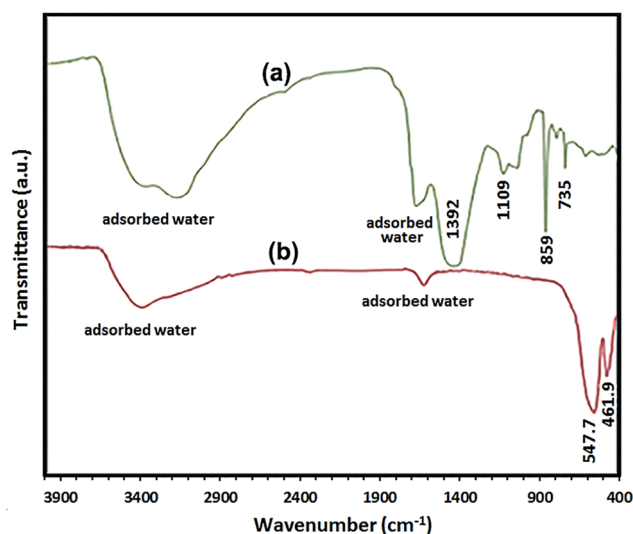


Fig. 7 FT-IR spectra of the as-synthesized FeCO_3 (a), and $\alpha\text{-Fe}_2\text{O}_3$ produced at 600°C (b).

at 1780 cm^{-1} may be ascribed to the overtone or combination of some vibrational frequencies of divalent metal cations and the carbonate group bond.^{5,11,12,40} The broad vibrational band at 3140 cm^{-1} and the band at 1660 cm^{-1} may be assigned to the stretching and the bending vibrations, respectively, of adsorbed water molecules interacting with CO_3^{2-} anions of the iron carbonate molecules.^{5,11,12,34}

3.1.4. Thermal study. The thermal conversion of the as-synthesized iron carbonate product was investigated using TG analysis, Fig. 8. Fig. 8 indicates the presence of 36.20% overall weight loss in two weight loss steps in the TG curve in the temperature ranges $25\text{--}100^\circ\text{C}$ and $120\text{--}350^\circ\text{C}$. The first weight loss, *ca.* 3.0% (theoretical value, 3.75%), may be assigned to the loss of adsorbed/trapped water molecules from the iron carbonate sample. Whereas, the second step, 33.20% (theoretical value, 33.66%) may be due to the thermal conversion of FeCO_3 into Fe_2O_3 , CO, and CO_2 under N_2 gas atmosphere. This

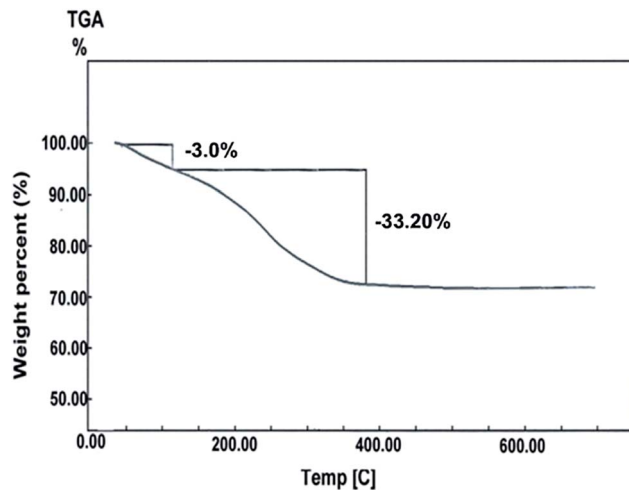


Fig. 8 Thermo-gravimetric analysis of the as-synthesized FeCO_3 under N_2 gas.

thermal behavior is similar to the that reported for CoCO_3 elsewhere.^{5,11,12}

3.2. Preparation and characterization of $\alpha\text{-Fe}_2\text{O}_3$ nanoparticles

Based on the aforementioned thermal data, the as-synthesized iron carbonate nanospheres, prepared at the optimized conditions, were thermally heated up at 400°C for 2 h to produce pure $\alpha\text{-Fe}_2\text{O}_3$ nanoparticles. Fig. 1(b) exhibits the XRD pattern of the iron oxide product and this pattern can be readily indexed to pure $\alpha\text{-Fe}_2\text{O}_3$ phase with the hexagonal structure (space group $R\bar{3}c$, lattice constant; $a = 5.038\text{ \AA}$ and $c = 13.776\text{ \AA}$, JCPDS card 89-0598). The estimated average crystallite size of the produced $\alpha\text{-Fe}_2\text{O}_3$ nanoparticles using the Debye–Scherrer equation³⁸ was found to be *ca.* 10.5 nm. Moreover, the as-prepared FeCO_3 precursor was also calcinated at 500 and 600°C to $\alpha\text{-Fe}_2\text{O}_3$ nanoparticles with different crystallite sizes; 19.8 and 31.2 nm, respectively, calculated from the XRD patterns of the produced $\alpha\text{-Fe}_2\text{O}_3$, Fig. 1(c) and (d), using the Debye–Scherrer equation. It is noticeable that higher calcination temperatures produced larger crystallite sizes. The surface morphology and microstructure of $\alpha\text{-Fe}_2\text{O}_3$ particles produced at 600°C and displayed in Fig. 6(II) and 9 have been investigated using FE-SEM and TEM, respectively. It can be seen from Fig. 6(II) that $\alpha\text{-Fe}_2\text{O}_3$ product is clusters of individually spherical shape $\alpha\text{-Fe}_2\text{O}_3$ particles and this indicates that iron carbonate morphologies on calcination have almost been retained for $\alpha\text{-Fe}_2\text{O}_3$ product. Inspection the size and morphology of the $\alpha\text{-Fe}_2\text{O}_3$ particles, Fig. 9, using TEM images exhibits that the $\alpha\text{-Fe}_2\text{O}_3$ product consists of irregular and spherical morphology with an average particle size of *ca.* 32 nm which is consistent with the one obtained using XRD data. Chemical structure of $\alpha\text{-Fe}_2\text{O}_3$ produced at 600°C ($\text{Fe}_2\text{O}_3\text{-}600$ product) was also confirmed by using Fourier transform infrared spectrum, Fig. 7(b), which exhibited two strong absorption bands at 547.7 and 461.9 cm^{-1} corresponding to the Fe–O bond which is consistent with the

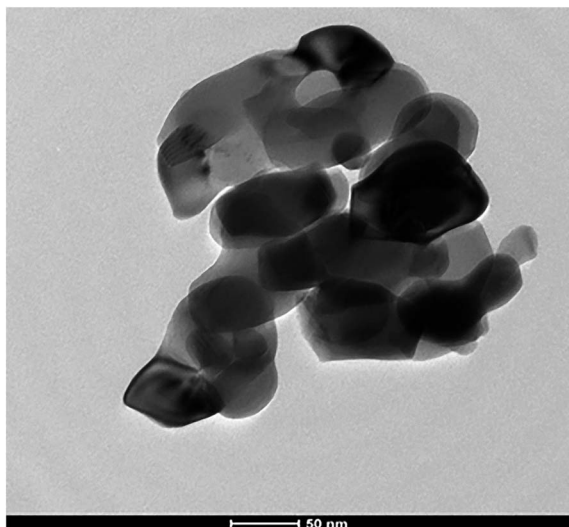


Fig. 9 HR-TEM image of the as-produced α -Fe₂O₃ nanoparticles produced at 600 °C.

published data.^{21,41,42} Plus, the two bands appeared at 3370 and 1600 cm⁻¹ can be attributed to the stretching and bending vibrations of adsorbed surface water molecules interacting with the oxide product and the broadness of these peaks may be assigned to hydrogen bonding O–H.³⁹

3.2.1. Point of zero charge (PZC) and isoelectric point (IEP). The point of zero charge (pH_{pzc}) of Fe₂O₃ nanoparticles calcinated at 600 °C (Fe₂O₃-600) was estimated by the pH drift method as reported by Ahmaruzzaman *et al.*⁴³ It is notably, pH_{pzc} is the pH at which charge on the Fe₂O₃ nanoparticles is zero. The pH_{pzc} of the Fe₂O₃ was determined as follows: 25 mLs of 0.01 M NaCl solution with initial pH ($\text{pH}_{\text{initial}}$) in the range between 2.0 and 10.0 adjusted with 0.1 M NaOH or 0.1 M HCl solution. Then, each NaCl solution (25 mL) was added to 0.05 g of the Fe₂O₃ adsorbent then left to stir for 48 h. The mixture was centrifuged and pH of the supernatant was measured (pH_{final}). Fig. 10(a), exhibits plotting of $\text{pH}_{\text{initial}}$ versus pH_{final} and the point at which the curve $\text{pH}_{\text{initial}} - \text{pH}_{\text{final}}$ intersects the $\text{pH}_{\text{initial}} = \text{pH}_{\text{final}}$ line is the pH_{pzc} . The pH_{pzc} value of the Fe₂O₃ adsorbent is estimated to be *ca.* 6.8 which is in agreement with the published data.^{44,45}

On the other hand, the pH of the isoelectric point (IEP) was determined by plotting the zeta potentials of Fe₂O₃ suspensions in 0.01 M NaCl solutions at various pH range from 2 to 10, as shown in Fig. 10(b). The pH was adjusted with 0.1 M NaOH or 0.1 M HCl solutions. The pH value of the isoelectric point (IEP) is found to be *ca.* 7.1 which is in consistent with the published data.^{44–46}

3.3. Adsorption properties of α -Fe₂O₃ nanoparticles

Adsorption properties of the α -Fe₂O₃ nanoparticles calcinated at 600 °C (Fe₂O₃-600) were investigated by choosing RR195 dye as an adsorbate model.

3.3.1. Effect of pH. Initial pH of the solution plays an important role in the adsorption experiments because it

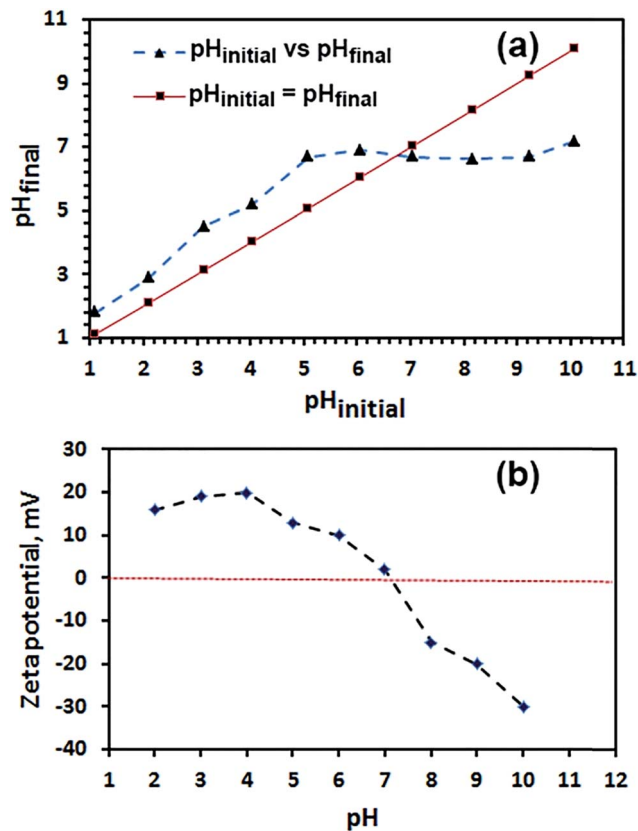


Fig. 10 $\text{pH}_{\text{initial}}$ against pH_{final} plot for determination of pH_{pzc} for of α -Fe₂O₃ nanoparticles (a), and zeta potential of α -Fe₂O₃ nanoparticles as a function of pH (b).

influences the surface binding sites of the nanoparticles acting as adsorbents and the dye speciation, as well. Effect of the initial pH of the solution on the adsorption of the RR195 dye ($C_0 = 20$ ppm, $\lambda_{\text{max}} = 542$ nm) on α -Fe₂O₃ nanoparticles ($m = 0.1$ g) for 24 h as contact time was investigated and presented in Fig. 11. The data exhibited that the adsorption was pH dependent and the maximum adsorption was observed to be in the range of pH 1–3. Afterwards, the adsorption decreased slowly by increasing pH up to almost 5 then decreased significantly at higher pH values. Therefore, the other adsorption experiments in this study were

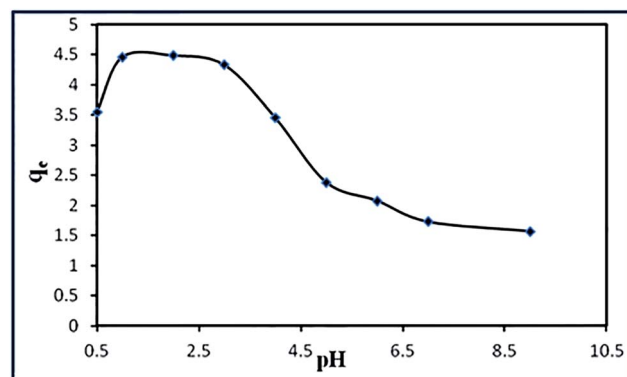


Fig. 11 pH influence on RR195 dye removal efficiency.

carried out at pH 2, as an optimized pH value. This phenomenon may be explained on the basis that at pHs lower than pH_{pzc} or IEP ($\text{pH}_{\text{pzc}} = 6.8$ and $\text{IEP} = 7.1$ for $\alpha\text{-Fe}_2\text{O}_3$ nanoparticles), the surface of the $\alpha\text{-Fe}_2\text{O}_3$ is positively charged and hence the attraction between the oppositely charges (*i.e.* these positively charges and the negatively charged RR195 dye) results in higher adsorption. Consequently, at pHs higher than pH_{pzc} or IEP there will be an electrostatic repulsion between the negatively charged $\alpha\text{-Fe}_2\text{O}_3$ surface and the negatively charged RR195 dye and this may be the reason for lower adsorption at higher pH values.

3.3.2. Effect of initial dye concentration. The dependence of the adsorption on the RR195 dye initial concentration (10–50 ppm) was investigated at room temperature and pH 2 and presented in Fig. 12. It can be clearly observe that the removal efficiency decreases from 95.5% to 42.6% with increasing the initial dye concentration from 10 ppm to 50 ppm, respectively. This may be attributed to saturation of the adsorption surface sites on the $\alpha\text{-Fe}_2\text{O}_3$ adsorbent on increasing the initial dye concentration.

3.3.3. Effect of ionic strength. The presence of dissolved inorganic ions is well known problem in wastewater containing industrial dyes.⁴⁷ These dissolved ions can compete with the dye of interest for the adsorption on the active sites on the adsorbent surface and hence this may reduce the adsorption efficiency of the dyes. In this study, influence of ionic strength by addition of KCl salt to the dye solution (30 ppm) on the adsorption process was investigated and presented in Fig. 13. The data indicate the decrease of the dye removal by increasing the KCl concentration because ions of the salt compete with the RR195 dye in adsorption by $\alpha\text{-Fe}_2\text{O}_3$ adsorbent.

3.3.4. Effect of contact time on the adsorption and the kinetic studies. The effect of contact time on the adsorption of RR195 dye was investigated at the optimized pH 2, 0.1 g adsorbent, and 10 ppm dye initial concentration, as shown in Fig. 14. It can be seen that the adsorption amount increased rapidly and reached about 95.5% in only 10 min and afterwards it stayed almost constant. Hence, 10 min was selected as the optimized contact time for the remaining study. This rapid adsorption may be attributed to the presence of large number of

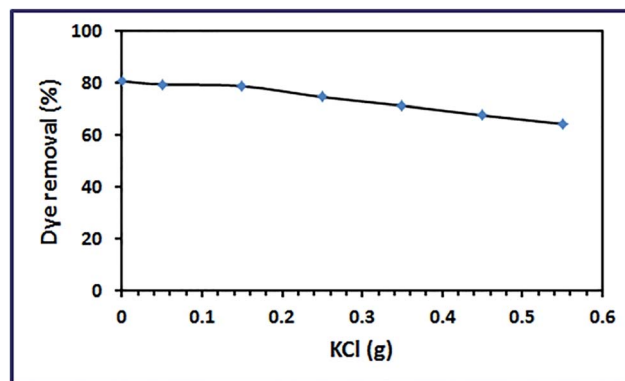


Fig. 13 Effect of KCl concentration on RR195 dye removal percentage.

surface sites for the $\alpha\text{-Fe}_2\text{O}_3$ nanoparticles available for adsorption.

To gain some information about the adsorbate amount and the rate of the adsorption process, kinetic parameters of RR195 dye adsorption on the $\alpha\text{-Fe}_2\text{O}_3$ adsorbent were calculated by applying pseudo-first order equation,⁴⁸ pseudo-second order equation,⁴⁹ and intraparticle diffusion model,⁵⁰ as shown in Fig. 15(a)–(c), respectively. It is noteworthy that the validity and fitting of the kinetic model can be examined by checking the value of the linear regression which is also known as a correlation coefficient, r^2 . The linear form of pseudo-first order kinetic model is:

$$\log(q_e - q_t) = \log q_e - \frac{k_1}{2.303} t \quad (3)$$

where k_1 (min^{-1}) is the pseudo-first order rate adsorption constant, q_e (mg g^{-1}) is the adsorption capacity at equilibrium, and q_t (mg g^{-1}) is the adsorption capacity at time t (min). Plus, values of k_1 can be determined from plotting of $\log(q_e - q_t)$ against t , Fig. 15(a). However, the obtained experimental data did not fit the pseudo-first order kinetic model, and the straight line could not be obtained, hence we tried to fit the adsorption data using pseudo-second order kinetic model. The linear form of the pseudo-second order kinetic equation can be given as follows:

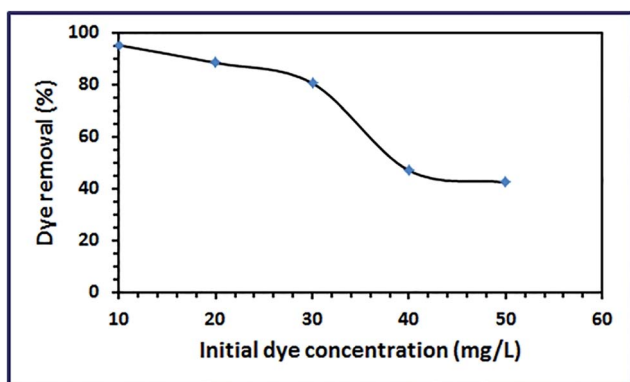


Fig. 12 Influence of initial RR195 dye concentration on its removal percentage.

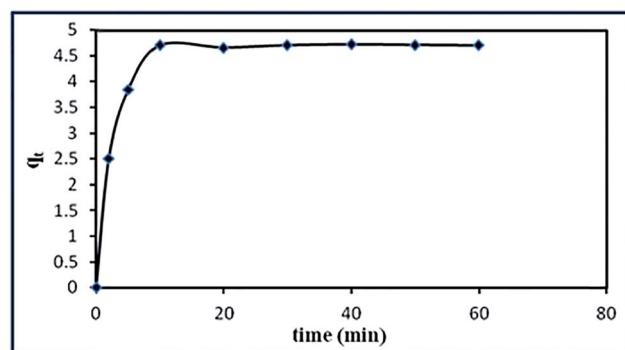


Fig. 14 Influence of contact time on RR195 dye adsorption by $\alpha\text{-Fe}_2\text{O}_3$ nanoparticles.

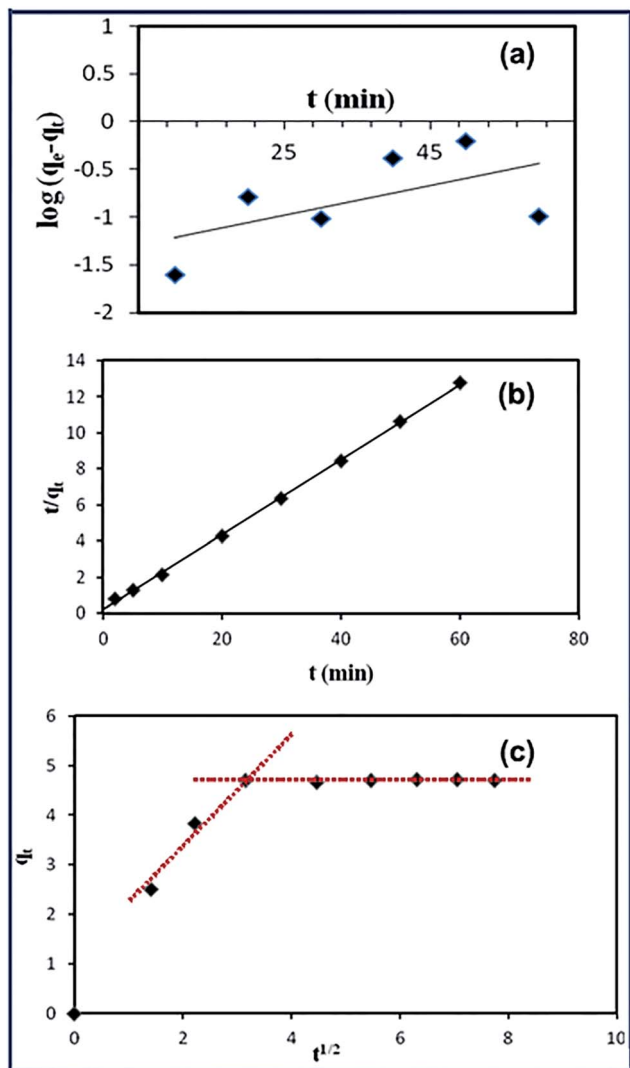


Fig. 15 Adsorption kinetic; (a) pseudo-first-order, (b) pseudo-second-order, and (c) intra-particle diffusion model, for RR195 dye adsorption onto α -Fe₂O₃ nanoparticles.

$$\frac{t}{q_t} = \frac{1}{k_2 q_e^2} + \frac{t}{q_e} \quad (4)$$

where k_2 ((g mg⁻¹) min) is the rate constant of pseudo-second order rate adsorption constant which can be calculated from plotting of t/q_t against t as shown in Fig. 15(b). The adsorption kinetic constants including the calculated equilibrium adsorption capacity $q_{e(\text{cal})}$ and the experimental equilibrium adsorption capacity $q_{e(\text{exp})}$ for the adsorption of RR195 dye on α -Fe₂O₃ adsorbent are presented in Table 1. Based on Fig. 15(a) and (b) and the values of the regression coefficients presented in Table 2, it is clearly obvious that the adsorption of RR195 dye on α -Fe₂O₃ adsorbent can be described well by pseudo-second order model. Plus, the experimental adsorption capacity value ($q_{e(\text{exp})}$) is consistent with the calculated one ($q_{e(\text{cal})}$). However, in order to gain further insight into the rate determining step involved in the adsorption of RR195 dye on α -Fe₂O₃ adsorbent, intra-particle diffusion model was examined by applying the Weber and Morris equation:

Table 2 Kinetic constants for RR195 dye adsorption on α -Fe₂O₃ nanoparticles

Kinetics models	Parameters	Value
Pseudo-first order	k_1 (min ⁻¹)	0.036
	$q_{e(\text{cal})}$ (mg g ⁻¹)	4.70
	r_1^2	0.339
Pseudo-second order	$q_{e(\text{exp})}$ (mg g ⁻¹)	0.042
	k_2 [g mg ⁻¹ min ⁻¹]	0.208
	$q_{e(\text{cal})}$ (mg g ⁻¹)	4.70
	r_2^2	0.999
	$q_{e(\text{exp})}$ (mg g ⁻¹)	4.81

$$q_t = k_i t^{0.5} + C \quad (5)$$

where k_i is the intra-particle diffusion constant (mg (g min^{1/2})⁻¹), and C represents the boundary layer thickness (mg g⁻¹). According to this model, plotting of q_t values against $t^{0.5}$ values should give a straight line which passes through the origin, if the rate determining step is the intra-particle diffusion. Otherwise, boundary layer diffusion or chemical reaction is the rate determining step. In the current case, the obtained plot (Fig. 15(c)) is a multilinear and does not passing the origin which indicates that the overall adsorption process may proceed by more than one mechanism such as film diffusion, chemical reaction, and intra-particle diffusion.⁵¹

3.3.5. Adsorption isotherms. Adsorption results have been analyzed using the two well-known isotherms; Langmuir and Freundlich models. These two models can be applied to describe the adsorption capacity of the adsorbent at different equilibrium concentrations of the dye at the optimized adsorption conditions. The linear form of the Langmuir relationship can be expressed as follows:

$$\frac{C_e}{q_e} = \frac{1}{K_L q_m} + \frac{C_e}{q_m} \quad (6)$$

where C_e is the equilibrium concentration of the RR195 dye in solution (mg L⁻¹), q_e is the equilibrium adsorption capacity of the RR195 dye on the α -Fe₂O₃ adsorbent, q_{max} is the maximum of adsorbed solute to form a monolayer per gram of adsorbent (mg g⁻¹), and K_L is the Langmuir adsorption constant (L mg⁻¹). The constants K_L and q_{max} can be calculated from the slope and intercept of the linear plot of C_e/q_e versus C_e (Fig. 16(a)). The linear form of the Freundlich isotherm can be given as follows:

$$\ln q_e = \ln K_F + \frac{1}{n} \ln C_e \quad (7)$$

where n and K_F are Freundlich constants related to adsorption intensity and adsorption capacity of the α -Fe₂O₃ adsorbent, respectively, and they are obtained from the slope and intercept of the linear plot of $\ln q_e$ against $\ln C_e$ (Fig. 16(b)). The Langmuir and Freundlich constants are presented in Table 3. Clearly, the adsorption of RR195 dye on the α -Fe₂O₃ adsorbent follows the Langmuir adsorption isotherm model and the correlation coefficient for this model is estimated to be 0.992. Plus, fitting of the experimental data to Langmuir isotherm model exhibits the homogeneous nature of α -Fe₂O₃ surface

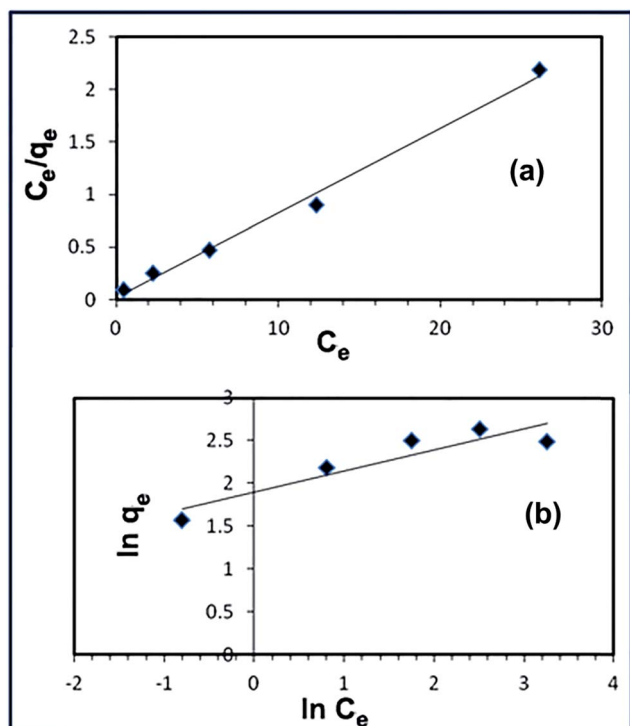


Fig. 16 Langmuir (a) and Freundlich (b) isotherms for RR195 dye adsorption onto α -Fe₂O₃ nanoparticles.

Table 3 Isotherm parameters for RR195 dye adsorption of on α -Fe₂O₃ nanoparticles

Isotherm models	Constants	Value
Langmuir	K_L (L mg ⁻¹)	3.23
	$q_{m(\text{cal})}$ (mg g ⁻¹)	4.87
	r_1^2	0.992
	R_L	0.0062
	$q_{e(\text{exp})}$ (mg g ⁻¹)	4.70
Freundlich	K_F (mg g ⁻¹) (L mg ⁻¹) ^{1/n}	6.65
	$q_{e(\text{cal})}$ (mg g ⁻¹)	20.7
	r_2^2	0.844
	n	4.02
	$q_{e(\text{exp})}$ (mg g ⁻¹)	4.70

which in turn means that each RR195 dye molecule/adsorption has equal activation energy of adsorption. Hence, the results reveal that the adsorption of the RR195 dye is monolayer coverage at the outer surface of α -Fe₂O₃ adsorbent. Moreover, the efficiency of the adsorption of the RR195 dye on the adsorbent can be estimated through the values of the separation factor constant (R_L) which can be given as follows:

$$R_L = \frac{1}{1 + K_L C_0} \quad (8)$$

where C_0 , and K_L are the initial concentration (mg L⁻¹) and the Langmuir constant (L mg⁻¹), respectively. The value of the R_L indicates whether the isotherm type is irreversible $R_L = 0$, favorable $0 < R_L < 1$, linear $R_L = 1$, or unfavorable $R_L > 1$. The calculated R_L value in the current case is found to be 0.00615

which refers to that the adsorption of the RR195 dye on the α -Fe₂O₃ adsorbent is favorable in this investigation at the optimized adsorption conditions.

3.3.6. Thermodynamic adsorption studies. Influence of the temperature on the adsorption process was investigated by studying the adsorption of RR195 dye on the α -Fe₂O₃ adsorbent at different temperatures; 303, 313, and 323 K. It is found that the adsorption capacity increases from 11.36 to 12.18 mg g⁻¹ on increasing temperature from 303 to 323 K. This is an indication that the adsorption of RR195 dye on α -Fe₂O₃ nanoparticles is an endothermic process. The thermodynamic parameters such as standard Gibbs free energy (ΔG^0), standard enthalpy (ΔH^0), and standard entropy (ΔS^0) can be estimated using the following equations:⁵²

$$\ln K_c = \frac{\Delta S^0}{R} - \frac{\Delta H^0}{RT} \quad (9)$$

$$\Delta G^0 = -RT \ln K_c \quad (10)$$

$$\Delta G^0 = \Delta H^0 - T\Delta S^0 \quad (11)$$

where K_c is the thermodynamic equilibrium constant (L g⁻¹) given by q_e/C_e , R is the universal gas constant (8.314 J mol⁻¹ K⁻¹), and T is the absolute solution temperature (K). As clear from eqn (9), plotting of $\ln K_c$ against $1/T$ gives a straight line (Fig. 17). ΔS^0 and ΔH^0 are calculated from the slope and

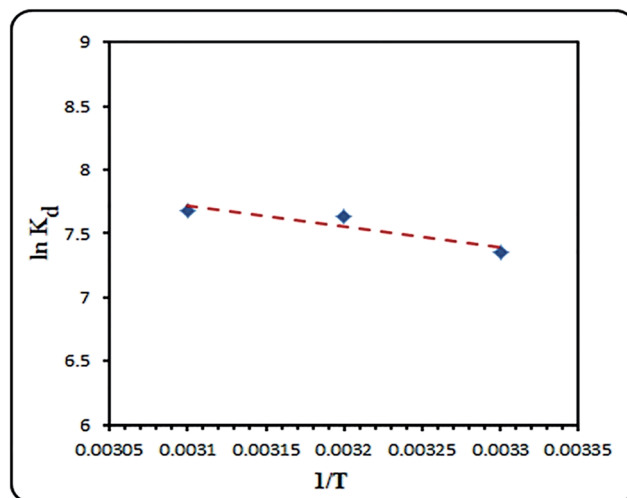


Fig. 17 Plot of $\ln K_c$ against $1/T$ for RR195 dye adsorption on α -Fe₂O₃ nanoparticles.

Table 4 Thermodynamic parameters for RR195 dye adsorption on α -Fe₂O₃ nanoparticles

Temperature (K)	$\ln K_c$	ΔG^0 (kJ mol ⁻¹)	ΔH^0 (kJ mol ⁻¹)	ΔS^0 (kJ mol ⁻¹ K ⁻¹)
303	10.20	-18.509	13.587	0.106
313	10.43	-19.851		
323	10.45	-20.609		

Table 5 BET surface area, pore size, pore volume, and crystallite size of Fe₂O₃ products and its removal capacity for RR195 dye

Adsorbent sample	BET surface area, m ² g ⁻¹	Crystallite size, nm	BJH pore diameter (nm)	BJH pore volume (cm ³ g ⁻¹)	Removal adsorption capacity (mg g ⁻¹)
Fe ₂ O ₃ -400	165.6	10.5	2.24	0.385	20.5
Fe ₂ O ₃ -500	130.3	19.8	2.02	0.266	9.6
Fe ₂ O ₃ -600	107.7	31.2	2.24	0.202	4.7

intercept, and presented in Table 4. Inspection of Table 4 reveals the endothermic nature of the adsorption process as indicated from the positive value of the ΔH^0 . Plus, the negative value of the ΔG^0 means that the adsorption of RR195 dye on the hematite nanoparticles is a spontaneous nature and the decrease in ΔG^0 values with increasing the temperature indicates that the adsorption process is more preferable at higher temperatures.

3.3.7. Surface area influence on the adsorption process and Fe₂O₃ adsorbent reusability. One of the factors that can influence on the adsorption process is the surface area of the adsorbents. The BET surface area (using nitrogen adsorption-desorption isotherms), BJH pore size, total pore volume, and crystallite size (calculated from the Debye-Scherrer equation) of the nano-sized products (Fe₂O₃-400, Fe₂O₃-500, and Fe₂O₃-600) were investigated and the results are tabulated in Table 5. The results exhibited that the order of BET surface areas for Fe₂O₃ products was Fe₂O₃-400 > Fe₂O₃-500 > Fe₂O₃-600. Also, the BJH pore volumes for the Fe₂O₃ nanostructures were in the same order.

However, as expected, the crystallite size of the aforementioned Fe₂O₃ products was in the reverse order. Moreover, in order to investigate the influence of the specific surface areas of the iron oxide products on the adsorption process, adsorption capacities of the products toward the RR195 dye were determined under the previously obtained optimum conditions and presented in Table 5. It is clear from this table that Fe₂O₃-400 adsorbent has the highest adsorption capacity (20.5 mg g⁻¹) and the order of the adsorption capacities of the iron oxide products is in the same order as that for the surface areas. This can be explained based on that the higher surface area provides

more contact and exposed sites for dye adsorption and hence this results in higher adsorption capacity.

On the other hand, reusability (*i.e.* recycling) of the adsorbents for industrial applications purposes is a crucial factor for choosing the suitable adsorbents. Hence, studying the recycling of the Fe₂O₃-400 adsorbent was performed by regenerating the RR195-loaded adsorbent using either stirring the iron oxide in methanol for 5 h, washing with methanol, and drying at 60 °C for *ca.* 5 h; or by carrying out combustion of the loaded adsorbent at 500 °C for 30 min. The adsorption of the dye at the optimum conditions and regeneration of the loaded adsorbent was repeated for five times and the percent RR195 dye removal efficiency for the five recycles was depicted in Fig. 18. The results indicate that even after five recycles, Fe₂O₃-400 adsorbent still has high adsorption efficiency (*ca.* 94% RR195 dye removal efficiency). The good reusability data suggest that the as-prepared iron oxide adsorbent is an efficient adsorbent and the data also support the long term use of the adsorbent in water treatment from RR195 dye.

4. Conclusion

In the present work, pure FeCO₃ nanospheres were successfully synthesized in high yield, smaller particle size, and different morphology on comparing to the literatures by hydrothermal reaction of iron sulfate, ascorbic acid as reducing agent, and ammonium carbonate at 140 °C for 1.5 h with molar ratio of 1 : 1 : 6, respectively. Afterwards, α -Fe₂O₃ nanoparticles were produced by heating of the as-prepared iron carbonate at 400, 500, or 600 °C for 2 h. The as-prepared products were characterized by means of FE-SEM, XRD, FT-IR, HR-TEM, BET, zeta potential, and thermal analysis. The adsorption properties of the as-prepared hematite nanoparticles were investigated using reactive red 195 (RR195) dye and the results exhibited good adsorption capacity of the nanosized adsorbent. Plus, the α -Fe₂O₃ nanoparticles produced at 400 °C have the highest adsorption capacity since they have the highest BET surface area. The adsorption data fitted very well with the Langmuir isotherm model indicating that the adsorption reaction was essentially monolayer. The spontaneous and endothermic natures of the adsorption process were confirmed from the thermodynamic studies.

Acknowledgements

The authors thank Benha University, Egypt, for providing the required financial support to perform this research work.

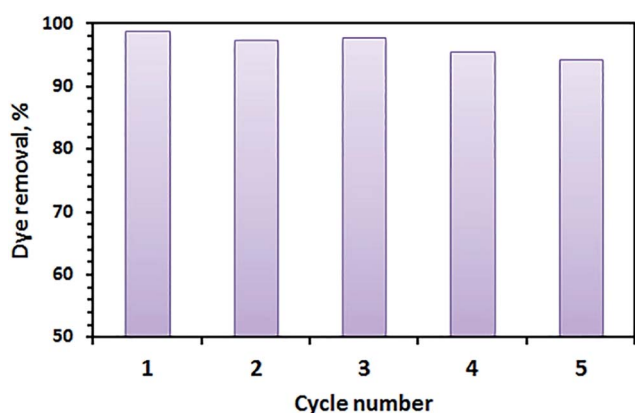


Fig. 18 RR195 dye removal efficiency of intact and regenerated α -Fe₂O₃ adsorbent during five adsorption/desorption cycles at 298 K.

References

- 1 S. Qadri, A. Ganoe and Y. Haik, Removal and recovery of acridine orange from solutions by use of magnetic nanoparticles, *J. Hazard. Mater.*, 2009, **169**(1–3), 318–323.
- 2 B. Tanhaei, A. Ayati, M. Lahtinen and M. Sillanpaa, Preparation and characterization of a novel chitosan/Al₂O₃/magnetite nanoparticles composite adsorbent for kinetic, thermodynamic and isotherm studies of methyl orange adsorption, *Chem. Eng. J.*, 2015, **259**, 1–10.
- 3 F. Qin, G. Li, H. Xiao, Z. Lu, H. Sun and R. Chen, Large-scale synthesis of bismuth hollow nanospheres for highly efficient Cr(vi) removal, *Dalton Trans.*, 2012, **41**, 11263–11266.
- 4 M. Y. Nassar and I. S. Ahmed, A novel synthetic route for magnesium aluminate (MgAl₂O₄) nanoparticles using sol-gel auto combustion method and their photocatalytic properties, *Spectrochim. Acta, Part A*, 2014, **131**, 320–334.
- 5 M. Y. Nassar and I. S. Ahmed, Template-free hydrothermal derived cobalt oxide nanopowders: synthesis, characterization, and removal of organic dyes, *Mater. Res. Bull.*, 2012, **47**, 2638–2645.
- 6 B. Bi, L. Xu, B. Xu and X. Liu, Heteropoly blue-intercalated layered double hydroxides for cationic dye removal from aqueous media, *Appl. Clay Sci.*, 2011, **54**, 242–247.
- 7 M. Khosravi and S. Azizian, Adsorption of anionic dyes from aqueous solution by iron oxide nanospheres, *J. Ind. Eng. Chem.*, 2014, **20**, 2561–2567.
- 8 H. Guo, J. Chen, W. Weng, Z. Zheng and D. Wang, Adsorption behavior of Congo red from aqueous solution on La₂O₃-doped TiO₂ nanotubes, *J. Ind. Eng. Chem.*, 2014, **20**, 3081–3088.
- 9 M. Y. Nassar, T. Y. Mohamed and I. S. Ahmed, One-pot solvothermal synthesis of novel cobalt salicylaldehyde-urea complexes: a new approach to Co₃O₄ nanoparticles, *J. Mol. Struct.*, 2013, **1050**, 81–87.
- 10 M. Y. Nassar, A. S. Attia, K. A. Alfalouh and M. F. El-Shahat, Synthesis of two novel dinuclear molybdenum(0) complexes of quinoxaline-2,3-dione: new precursors for preparation of α -MoO₃ nanoplates, *Inorg. Chim. Acta*, 2013, **405**, 362–367.
- 11 M. Y. Nassar, Size-controlled synthesis of CoCO₃ and Co₃O₄ nanoparticles by free-surfactant hydrothermal method, *Mater. Lett.*, 2013, **94**, 112–115.
- 12 M. Y. Nassar and I. S. Ahmed, Hydrothermal synthesis of cobalt carbonates using different counter ions: an efficient precursor to nano-sized cobalt oxide (Co₃O₄), *Polyhedron*, 2011, **30**, 2431–2437.
- 13 T. G. Venkatesha, R. Viswanatha, Y. A. Nayaka and B. K. Chethana, Kinetics and thermodynamics of reactive and vat dyes adsorption on MgO nanoparticles, *Chem. Eng. J.*, 2012, **198–199**, 1–10.
- 14 H. Emadi and A. N. Kharat, Synthesis and characterization of ultrafine and mesoporous structure of cobalt ferrite, *J. Ind. Eng. Chem.*, 2015, **21**, 951–956.
- 15 Z. Zhang and J. Kong, Novel magnetic Fe₃O₄@C nanoparticles as adsorbents for removal of organic dyes from aqueous solution, *J. Hazard. Mater.*, 2011, **193**, 325–329.
- 16 H. Li, Z. Lu, G. Cheng, K. Rong, F. Chen and R. Chen, HEPES-involved hydrothermal synthesis of Fe₃O₄ nanoparticles and their biological application, *RSC Adv.*, 2015, **5**, 5059–5067.
- 17 H. Li, Z. Lu, Q. Li, M.-H. So, C.-M. Che and R. Chen, Hydrothermal synthesis and properties of controlled α -Fe₂O₃ nanostructures in HEPES solution, *Chem.-Asian J.*, 2011, **6**, 2320–2331.
- 18 H. Liang, W. Chen, Y. Yao, Z. Wang and Y. Yang, Hydrothermal synthesis, self-assembly and electrochemical performance of α -Fe₂O₃ microspheres for lithium ion batteries, *Ceram. Int.*, 2014, **40**, 10283–10290.
- 19 A. S. Teja and P. Y. Koh, Synthesis, properties, and applications of magnetic iron oxide nanoparticles, *Prog. Cryst. Growth Charact. Mater.*, 2009, **55**, 22–45.
- 20 M. Khalil, J. Yu, N. Liu and R. L. Lee, Non-aqueous modification of synthesized hematite nanoparticles with oleic acid, *Colloids Surf., A*, 2014, **453**, 7–12.
- 21 M. Mohammadikish, Hydrothermal synthesis, characterization and optical properties of ellipsoid shape α -Fe₂O₃ nanocrystals, *Ceram. Int.*, 2014, **40**, 1351–1358.
- 22 M.-C. Huang, The optical, structural and photoelectrochemical characteristics of porous hematite hollow spheres prepared by DC magnetron sputtering process via polystyrene spheres template, *Ceram. Int.*, 2014, **40**, 10537–10544.
- 23 J. Xie, Z. Zhou, Y. Lian, Y. Hao, P. Li and Y. Wei, Synthesis of α -Fe₂O₃/ZnO composites for photocatalytic degradation of pentachlorophenol under UV-vis light irradiation, *Ceram. Int.*, 2015, **41**, 2622–2625.
- 24 M. Gotić, G. Dražić and S. Musić, Hydrothermal synthesis of α -Fe₂O₃ nanorings with the help of divalent metal cations, Mn²⁺, Cu²⁺, Zn²⁺ and Ni²⁺, *J. Mol. Struct.*, 2011, **993**, 167–176.
- 25 C. Wu, P. Yin, X. Zhu, C. O. Yang and Y. Xie, Synthesis of hematite (α -Fe₂O₃) nanorods: diameter-size and shape effects on their applications in magnetism, lithium ion battery, and gas sensors, *J. Phys. Chem. B*, 2006, **110**, 17806–17812.
- 26 S. Rahimi, R. M. Moattaria, L. Rajabia, A. A. Derakhshanb and M. Keyhani, Iron oxide/hydroxide (α , γ -FeOOH) nanoparticles as high potential adsorbents for lead removal from polluted aquatic media, *J. Ind. Eng. Chem.*, 2015, **23**, 33–43.
- 27 H. Wu, G. Wu and L. Wang, Peculiar porous α -Fe₂O₃, γ -Fe₂O₃ and Fe₃O₄ nanospheres: facile synthesis and electromagnetic properties, *Powder Technol.*, 2015, **269**, 443–451.
- 28 G. Wu, X. Tan, G. Li and C. Hu, Effect of preparation method on the physical and catalytic property of nanocrystalline Fe₂O₃, *J. Alloys Compd.*, 2010, **504**, 371–376.
- 29 A. A. Ayachia, H. Mechakra, M. M. Silvan, S. Boudjaadar and S. Achour, Monodisperse α -Fe₂O₃ nanoplatelets: synthesis and characterization, *Ceram. Int.*, 2015, **41**, 2228–2233.
- 30 T.-W. Sun, Y.-J. Zhu, C. Qi, G.-J. Ding, F. Chen and J. Wu, α -Fe₂O₃ nanosheet-assembled hierarchical hollow mesoporous microspheres: microwave-assisted solvothermal synthesis and application in photocatalysis, *J. Colloid Interface Sci.*, 2016, **463**, 107–117.

- 31 X.-L. Cheng, J.-S. Jiang, C.-Y. Jin, C.-C. Lin, Y. Zeng and Q.-H. Zhang, Cauliflower-like α -Fe₂O₃ microstructures: toluene–water interface assisted synthesis, characterization, and applications in wastewater treatment and visible-light photocatalysis, *Chem. Eng. J.*, 2014, **236**, 139–148.
- 32 S. Sivakumar, D. Anusuya, C. P. Khatiwada, J. Sivasubramanian, A. Venkatesan and P. Soundhirarajan, Characterizations of diverse mole of pure and Ni-doped α -Fe₂O₃ synthesized nanoparticles through chemical precipitation route, *Spectrochim. Acta, Part A*, 2014, **128**, 69–75.
- 33 D. Wang, M. Zhang, J. Yuan, Y. Lin and C. Song, Facile route to Ni-doped α -FeOOH and α -Fe₂O₃ nanostructures and their properties, *Mater. Lett.*, 2015, **157**, 147–150.
- 34 X. J. Liu, H. Wang, C. H. Su, P. W. Zhang and J. B. Bai, Controlled fabrication and characterization of microspherical FeCO₃ and α -Fe₂O₃, *J. Colloid Interface Sci.*, 2010, **351**, 427–432.
- 35 S. Xuan, M. Chen, L. Hao, W. Jiang, X. Gong, Y. Hu and Z. Chen, Preparation and characterization of microsized FeCO₃, Fe₃O₄ and Fe₂O₃ with ellipsoidal morphology, *J. Magn. Magn. Mater.*, 2008, **320**, 164–170.
- 36 T. Yang, Z. Huang, Y. Liu, M. Fang, X. Ouyang and M. Hu, Controlled synthesis of porous FeCO₃ microspheres and the conversion to α -Fe₂O₃ with unconventional morphology, *Ceram. Int.*, 2014, **40**, 11975–11983.
- 37 M. Chirita and A. Ieta, FeCO₃ microparticle synthesis by Fe–EDTA hydrothermal decomposition, *Cryst. Growth Des.*, 2012, **12**, 883–886.
- 38 R. Jenkins and R. L. Snyder, *Chemical Analysis: Introduction to X-ray Powder Diffractometry*, John Wiley and Sons, Inc., New York, 1996.
- 39 K. Nakamoto, *Infrared and Raman spectra of inorganic and coordination compounds; Pt. B: Applications in coordination, organometallic, and bioinorganic chemistry*, Wiley-Interscience, USA, 5th edn, 1997.
- 40 K. T. Ehlsissen, A. Delahaya-Vidal, P. Genin, M. Figlarz and P. Willmann, Preparation and characterization of turbostratic Ni/Al layered double hydroxides for nickel hydroxide electrode applications, *J. Mater. Chem.*, 1993, **3**, 883–888.
- 41 R. Suresh, K. Giribabu, R. Manigandan, A. Stephen and V. Narayanan, Fe₂O₃@polyaniline nanocomposite: characterization and unusual sensing property, *Mater. Lett.*, 2014, **128**, 369–372.
- 42 R. A. Bepari, P. Bharali and B. K. Das, Controlled synthesis of α and γ -Fe₂O₃ nanoparticles *via* thermolysis of PVA gels and studies on α -Fe₂O₃ catalyzed styrene epoxidation, *J. Saudi Chem. Soc.*, 2014, DOI: 10.1016/j.jscs.2013.12.010.
- 43 M. Ahmaruzzaman and S. L. Gayatri, Batch adsorption of 4-nitrophenol by acid activated jute stick char: equilibrium, kinetic and thermodynamic studies, *Chem. Eng. J.*, 2010, **158**, 173–180.
- 44 M. Kosmulski, pH-dependent surface charging and points of zero charge II. Update, *J. Colloid Interface Sci.*, 2004, **275**, 214–224.
- 45 M. Kosmulski, E. Maczka, E. Jartych and J. B. Rosenholm, Synthesis and characterization of goethite and goethite–hematite composite: experimental study and literature survey, *Adv. Colloid Interface Sci.*, 2003, **103**, 57–76.
- 46 E. Liu, H. Zhao, H. Li, G. Li, Y. Liu and R. Chen, Hydrothermal synthesis of porous α -Fe₂O₃ nanostructures for highly efficient Cr(vi) removal, *New J. Chem.*, 2014, **38**, 2911–2916.
- 47 N. M. Mahmoodi and F. Najafi, Preparation of surface modified zinc oxide nanoparticle with high capacity dye removal ability, *Mater. Res. Bull.*, 2012, **47**, 1800–1809.
- 48 M. N. Sepehr, V. Sivasankar, M. Zarrabi and M. S. Kumar, Surface modification of pumice enhancing its fluoride adsorption capacity: an insight into kinetic and thermodynamic studies, *Chem. Eng. J.*, 2013, **228**, 192–204.
- 49 Y. S. Ho and G. McKay, Pseudo-second order model for sorption processes, *Process Biochem.*, 1999, **34**, 451–465.
- 50 W. J. Weber Jr and J. C. Morris, Kinetics of adsorption on carbon from solution, *J. Sanit. Eng. Div., Am. Soc. Civ. Eng.*, 1963, **89**, 31–59.
- 51 C. Luo, Z. Tian, B. Yang, L. Zhang and S. Yan, Manganese dioxide/iron oxide/acid oxidized multi-walled carbon nanotube magnetic nanocomposite for enhanced hexavalent chromium removal, *Chem. Eng. J.*, 2013, **234**, 256–265.
- 52 J. Zhou, Z. Zhang, B. Cheng and J. Yu, Glycine-assisted hydrothermal synthesis and adsorption properties of crosslinked porous α -Fe₂O₃ nanomaterials for *p*-nitrophenol, *Chem. Eng. J.*, 2012, **211–212**, 153–160.